



Cite this: *Nanoscale*, 2015, 7, 19027

Supersonically blown nylon-6 nanofibers entangled with graphene flakes for water purification†

Jong-Gun Lee,^a Do-Yeon Kim,^a Mukund G. Mali,^a Salem S. Al-Deyab,^b Mark T. Swihart^c and Sam S. Yoon*^a

Water purification membranes, capable of purifying a few to tens of milliliters of aqueous methylene blue solution in a minute, were produced by supersonically blowing graphene flakes with a nylon-6 polymeric solution. The solution-blown nylon-6 nanofibers became entangled with graphene flakes thereby locking the graphene flakes within the frame of the bendable two-dimensional film structure. This method, which yielded a $5 \times 7 \text{ cm}^2$ -sized membrane in less than 10 seconds, is commercially viable owing to fast fabrication and scalability. We show that our water purification device allows a flow rate range of $0.3\text{--}4 \text{ L h}^{-1}$ with a membrane area of just 5 cm^2 , under a pressure difference of $0.5\text{--}3.5 \text{ bar}$. If the membrane were scaled up to 0.5 m^2 , it could provide $300\text{--}4000 \text{ L h}^{-1}$ flow rate, an ample supply for home use.

Received 22nd September 2015,
Accepted 13th October 2015

DOI: 10.1039/c5nr06549f

www.rsc.org/nanoscale

1. Introduction

Pure water is a basic human need, and technologies for water purification are required over a wide range of scales and applications from drinking water to irrigation to recovery of wastewater from hydrofracking. Currently, effluents containing organic dyes from the textile, printing, and dyeing industries are a serious environmental concern. Methylene blue (MB) is a prototypical synthetic organic dye that has been used for various applications including dyeing of cotton and wool, coating and coloring of paper, and as a hair colorant. MB and similar organic dyes are, in general, not readily biodegradable. Hence, many traditional water treatments fail to remove MB. Highly efficient and cost-effective techniques for removal of organic dye impurities are needed to address this issue.

As one means of addressing this need, composites containing carbonaceous materials such as graphene, carbon nanotubes, and carbon nanofibers for use in water purification have attracted significant attention from the scientific and engineering communities.^{1–4} For example, Grossman *et al.*⁵ showed computationally that NaCl (*i.e.*, salt ions) can be

efficiently removed from seawater by controlling the pore size of nanoporous graphene membranes such that only the passage of water molecules is allowed. Zhang *et al.*⁶ achieved 80% photo-degradation of an aqueous methylene blue solution in 1 h under ultraviolet (UV) illumination using titania (P25)–graphene composites. Similarly, Gupta *et al.* synthesized graphene from cane-sugar and studied its water purification efficiency by adsorption of rhodamine 6G from an aqueous solution.⁷ Liu *et al.* also studied the adsorption capability of graphene by dispersing graphene flakes with aqueous methylene blue, in what is considered a mobilized or dispersed method of water purification, which requires collection of dispersed adsorbents afterward.⁸ Crock *et al.* prepared polymer nanocomposite membranes by loading exfoliated graphite nanoplatelets decorated with Au nanoparticles into a multicomponent polymer membrane and achieved a permeability up to about $140 \text{ L h}^{-1} \text{ m}^{-2} \text{ bar}^{-1}$.⁹ Sui *et al.* prepared carbon nanotube–graphene hybrid aerogels *via* a green approach and studied their water purification performance. Their composite showed 633.3 mg g^{-1} desalination capacity.¹⁰ Singh *et al.* showed the removal of disinfection byproducts using a carbonized electrospun nanofiber membrane.¹¹

Despite the novelty of these previous studies, mobilized or dispersed methods are impractical from the viewpoint of commercialization, and studies of desalination *via* graphene have been mainly focused on computations.^{12–19} Purification by short-term (*i.e.*, for a few hours) UV irradiation of a relatively small amount of waste-water also lacks commercial feasibility. In fact, a practical membrane-based water purification device should allow a minimum flow rate of a few liters per hour (or

^aSchool of Mech. Eng., Korea University, Seoul 136-713, Korea.

E-mail: skyoon@korea.ac.kr

^bPetrochem. Research Chair, Dept. of Chem., King Saud Univ., Riyadh 11451, Saudi Arabia

^cDept. of Chemistry & Biological Eng., University at Buffalo (SUNY), Buffalo, NY, USA

†Electronic supplementary information (ESI) available. See DOI: 10.1039/c5nr06549f

tens of milliliters per min, because $1 \text{ L h}^{-1} \sim 17 \text{ mL min}^{-1}$) per cm^2 of the membrane area under a pressure difference of 1–2 bar, especially in the case of emergency or lifesaving situations. Therefore, the fabrication of a light, thin, small, and most importantly, portable membrane capable of supplying sufficient amounts of purified water is essential.

Recently, Yoon *et al.*²⁰ demonstrated the gravity-driven separation of oil from water and the purification of water using a superhydrophilic–oleophobic membrane with a graphene plug that allowed a flow rate of $0.167 \text{ mL min}^{-1}$. Here, we fabricated a significantly thinner membrane that allows an order of magnitude higher flow rate (of a few milliliters per min) and has purification performance equivalent to the graphene plug used in the previous study. We fabricated a high-concentration graphene membrane by supersonically blowing graphene flakes with a polymeric solution such that the solution-blown nanofibers become entangled with the graphene flakes.^{21–24} This method of fabrication locks the graphene flakes within the framework of the light and flexible 2D sheet membrane and has potential as a commercially-viable membrane fabrication method owing to the $<10 \text{ s}$ coating time required for a $5 \times 7 \text{ cm}^2$ substrate. Different concentrations of graphene were deposited on the $5 \times 7 \text{ cm}^2$ substrate by varying the deposition time. The fabricated water-purification graphene films were examined *via* scanning electron microscopy (SEM), thermogravimetric analysis (TGA), optical absorbance, and X-ray photoelectron spectroscopy (XPS) measurements.

2. Experimental details

2.1 Cold spray process

Fig. 1 shows the supersonic coating system. The powder feeder supplies graphene flakes, and air is provided *via* the compressor at 3 bar (gauge pressure) to the nozzle. The air is heated at $200 \text{ }^\circ\text{C}$ prior to reaching the nozzle. This gas accelerates in the converging section of the nozzle, reaches sonic velocity at the throat of the nozzle, and finally reaches supersonic speed as it expands in the diverging section of the nozzle. The gas is cooled as thermal energy is converted into kinetic energy. The

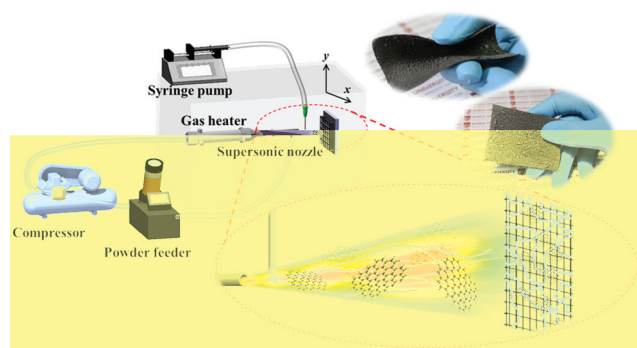


Fig. 1 Schematic of the supersonic kinetic spraying process for the fabrication of the nylon–graphene composite.

Table 1 Operating conditions for the supersonic-deposition spray system

Operating parameters	
Operating pressure [bar]	3
Propellant gas	Air
Nozzle exit diameter [mm]	8
Nozzle throat diameter [mm]	6
Nozzle-to-substrate distance [mm]	70
Gas temperature [K]	473

supersonic flow attains its highest speed at the nozzle exit.^{25–27} Table 1 summarizes the operating conditions and nozzle geometry. Simultaneously, the viscous solution of nylon-6 (15 wt% concentration), supplied to the supersonic stream by using a syringe pump, undergoes shear thinning and stretching, producing nanofibers. The graphene flakes, which enter the supersonic gas flow before the polymer, become entangled with the nylon-6 nanofibers and form a membrane or film upon impact with the stainless-steel mesh attached to the moving x - y stage. A stainless-steel mesh was used to support supersonically blown graphene/nylon-6 as a substrate. The membrane cannot readily be produced without a substrate because the graphene/nylon-6 alone is mechanically too weak to sustain itself as a rigid membrane.²⁴ During supersonic solution blowing, the nozzle was swept over the membrane vertically and horizontally multiple times to ensure uniform thickness of the membrane. Further details of the solution blowing technique are available in our previous publications.²⁴

2.2 Membrane materials

Graphene nanoplatelets (Grade M25, $D_a \sim 25 \mu\text{m}$, $<1.0 \text{ wt}\%$ oxygen) were purchased from XG Sciences, Inc. (USA). In the context of the standardized naming of carbon nanomaterials, these could be considered multi-layer graphene or graphite nanoplates,²⁸ but are termed graphene nanoplatelets by the manufacturer. The nylon-6 (Sigma Aldrich, the molecular weight of the repeating unit is 104.83 Da) solution was obtained by 24 h magnetic stirring of the corresponding pellets (15%) into formic acid (Sigma Aldrich). This polymer solution was supplied at a feed rate of $Q = 0.6 \text{ mL min}^{-1}$. The graphene flakes were supplied through a powder feeder (Praxair 1264i, USA) at a rate of $Q = 0.01 \text{ g min}^{-1}$. The graphene carrier air flow rate was $Q = 0.7 \text{ m}^3 \text{ min}^{-1}$. The needle (EFD, 18 gauge) of the syringe pump (KDS LEGATO 100) had inner and outer diameters of 0.84 and 1.27 mm, respectively. Here we refer to the membranes fabricated with deposition times of 10, 20, and 30 s as low, medium, and high graphene concentration membranes, respectively. Note that both the mass fraction of graphene and the total membrane thickness increase from 10 to 30 s deposition time.

2.3 Water purification

The water purification performance of the membrane was determined by using a methylene blue solution (#M2661,

0.1 wt% solution in water, Samchun Chemical, Suncheon, Korea), which was mixed with deionized water in a volume ratio of 1 : 200 to produce a 5 ppm solution. The syringe pump was used to push this model pollutant through the multiple graphene–nylon membranes at flow rates ranging from 0.6–30 mL min⁻¹; the solution was decolorized upon passing each membrane. The purified MB solution was collected at each passing and the corresponding degree of decoloration was measured by UV-visible absorbance spectroscopy (OPTIZEN POP, Mecasys Co. LTD, KOREA, 190 ≤ λ ≤ 1100 nm). The MB concentration is proportional to the absorbance at a wavelength of 664 nm.

2.4 Materials characterization

The surface morphologies and the inclusion of nylon-6 in, the membranes were imaged and confirmed, respectively, using a scanning electron microscope (HRSEM, XL30SFEG; Philips Co., Amsterdam, Holland) and a thermogravimetric analyzer (TGA, Q500, TA Instruments, USA). In addition, X-ray photoelectron spectroscopy (XPS, PHI5600, Physical Electronics) was used to determine the elemental compositions and identify the peaks corresponding to graphene and nylon-6. The BET surface area of graphene/nylon-6 was determined from N₂ physisorption analysis carried out at 77 K using a Micromeritics (Tristar 3000) BET analyzer. Raman spectroscopy (LabRam ARAMIS IR2, Horiba, Japan) was used to analyze the crystal quality of the kinetically-sprayed graphene flakes on the stainless steel substrate.

3. Results and discussion

3.1 Materials characterization

In this study, the supersonic blowing technique facilitated the production of nylon-6 nanofibers entangled with graphene flakes. The morphology of the nanocomposite films was studied by scanning electron microscopy, as shown in Fig. 2.

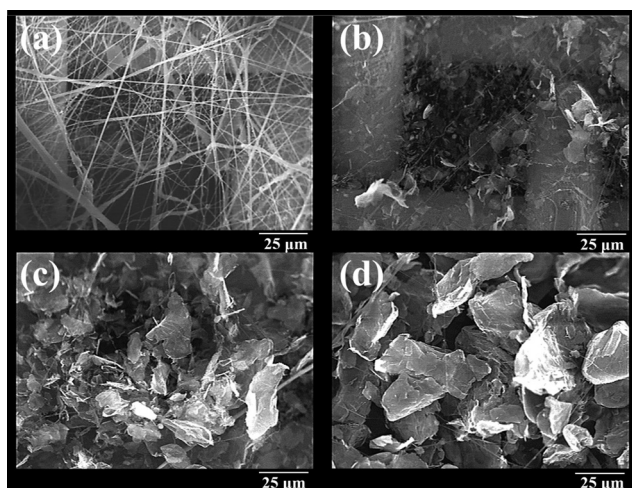


Fig. 2 Nylon-6 nanofibers (a) only, and with (b) low, (c) medium, and (d) high concentrations of graphene.

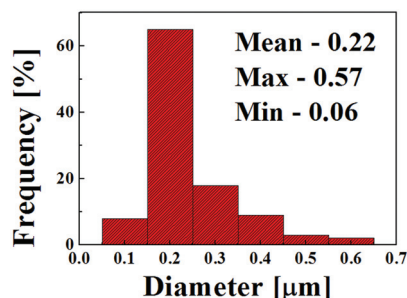


Fig. 3 Nylon-6 fiber size distribution.

Nylon-6 was chosen as a polymer component of these membranes because of its outstanding polymorphic and poly-electrolytic properties^{29,30} and also its high tensile strength, elasticity, and chemical resistance to both acids and bases. Fig. 2a shows an SEM image of the stainless steel mesh substrate coated with nylon-6 nanofibers without graphene flakes. Fig. 3 displays the fiber size distribution of the nylon-6, which was measured by using I-measure software 3.0 (INGPLUS). These nanofibers range from 60–570 nm in size, and have an average size of 220 nm. This size range is quite small, even when compared to electrospun nanofibers, which typically have diameters of a few hundred nanometers. Thus, the current fabrication method with supersonic blowing maximizes the functionality of the graphene flakes by minimizing the space occupied by the thin nanofibers, therefore enhancing the graphene's adsorption capability. A relatively large content of nanofibers inside the membrane could hinder the graphene's adsorption capability. When the stainless substrate is coated with nylon-6 nanofibers without graphene flakes, the membrane possesses no purification capability. On the other hand, graphene flakes alone cannot be deposited onto the substrate without nylon-6 fibers, which hold graphene flakes together.

Fig. 2b–d show the expected progressive accumulation of the graphene flakes with increasing deposition time (t_{dep}). The high nanofiber content, which is particularly evident for low t_{dep} (*i.e.*, short deposition time), is significantly reduced for high t_{dep} . Although both nylon and graphene are supplied at constant rates during the deposition, the deposition efficiency of the graphene increases as the membrane becomes thicker and the nanofiber network becomes denser. The low nylon content and the correspondingly large total mass of graphene resulting from high t_{dep} are desirable for water purification purposes.

Fig. 4 shows cross-sectional views of the low, medium, and high concentration membranes whose thickness was 168, 516, and 791 μm, respectively. Solution-blown nanofibers are entangled with the densely stacked graphene flakes. This entanglement holds graphene flakes quite tightly, which ensures the mechanical stability of the membrane. Porosity is relatively low, and thus relatively high pressure must be applied to pass water through the membrane, as discussed in detail below. However, this low porosity and small pore size

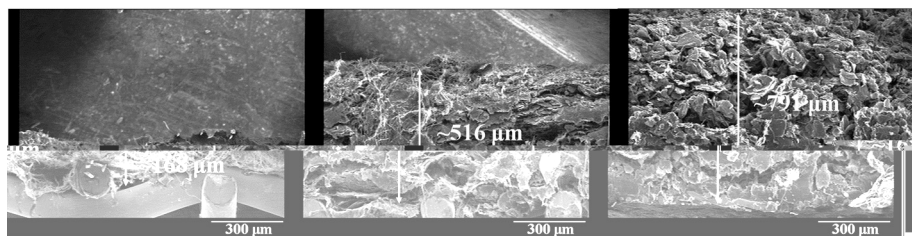


Fig. 4 SEM cross-sectional views of the membranes whose thickness is 168, 516, and 768 μm for the low, medium, and high concentration cases, respectively.

also ensure good contact between the water passing through the membrane and the graphene on which contaminants are adsorbed.

High resolution transmission electron microscopy (HR-TEM) images were obtained using a JEOL JEM-2100F microscope at 200 kV. The membranes were transferred to a nickel-TEM grid. Fig. 5a shows a TEM image of the low graphene/nylon-6. It shows the graphene sheet covered with nylon-6 nanofibers. The fiber diameter is around 0.25 μm . Fig. 5b also shows the SAED pattern of graphene. Fig. 5c and d show the SAED pattern of nylon-6 nanofibers and graphene/nylon-6 (low concentration case), respectively. The SAED pattern of graphene shows the inner ring attributed to the (110) plane while the outer ring is due to the (210) plane. Due to the amorphous state of nylon-6, it presents a featureless SAED pattern (Fig. 5c).

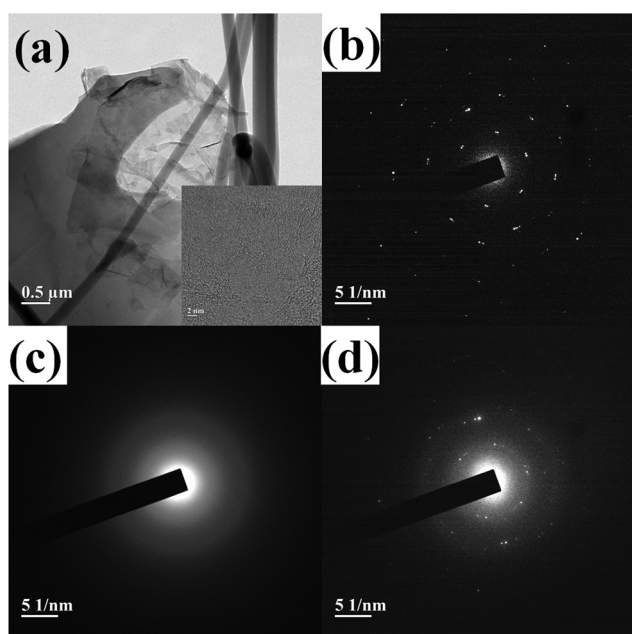


Fig. 5 (a) TEM image of graphene/nylon-6. (b) SAED pattern of graphene, (c) SAED pattern of nylon-6, (d) SAED pattern of graphene/nylon-6 (low concentration case).

To characterize the membrane comprised of graphene and nylon-6, Raman spectra of these materials before and after their deposition are shown in Fig. 6a and b, respectively. The two dominant peaks attributed to graphene are observed at $\sim 1579\text{ cm}^{-1}$ (G band) and $\sim 2718\text{ cm}^{-1}$ (2D band) with a relatively low peak at $\sim 1348\text{ cm}^{-1}$ (D band). The D and 2D bands are due to the presence of defects and the second-order zone boundary phonons, respectively, while the G band of graphene is related to the double-degenerate E_{2g} mode.³¹ The low D peak indicates that the graphene flakes are of high quality with a relatively low concentration of defects. The three dominant peaks corresponding to nylon-6 are found at 2900 cm^{-1} (CH_2 stretching band), 1634 cm^{-1} (amide I band), and 1440 cm^{-1} (CH_2 bending band).³² All of the expected peaks corresponding to graphene and nylon-6 are present in the deposited membrane, as confirmed in Fig. 6b.

Fig. 7 shows the results of the thermogravimetric analysis (TGA) of the low, medium, and high t_{dep} films, illustrating the decreasing mass fraction of the volatile material with increasing deposition time. For these estimations, the samples (consisting of graphene flakes and nylon-6 nanofibers, $\sim 3\text{ mg}$) were placed in a 7 mm sized disk holder, which was sealed with a cap. The TGA data were acquired (2050 TGA, TA Instruments) under a nitrogen atmosphere at a heating rate of $10\text{ }^\circ\text{C min}^{-1}$ for temperatures ranging from 30–800 $^\circ\text{C}$. As Fig. 7 shows, the nylon-6 nanofibers decompose at temperatures ranging from 350–400 $^\circ\text{C}$,^{4,33} and the membranes with low, medium, and high concentrations of graphene exhibit weight losses of 26.8%, 20.2%, and 9.2%, respectively. The graphene flakes, which are stable in nitrogen up to much higher temperatures, remain present after the nylon-6 has fully pyrolyzed. These TGA data confirm that the relative concentration of graphene flakes increases with increasing deposition time. More importantly, they show that graphene is the primary component of the film, present in substantially greater amounts than the nylon fibers which serve as a binder for the graphene flakes.

Fig. 8 displays typical nitrogen adsorption–desorption isotherms for the graphene/nylon-6 composite, from which we obtained its BET surface area. The isotherm exhibits an H3 type hysteresis loop starting from ~ 0.4 relative pressure, while at a lower relative pressure it exhibits typical type-1 behavior. Such a hysteresis loop in the isotherm demonstrates the micro-

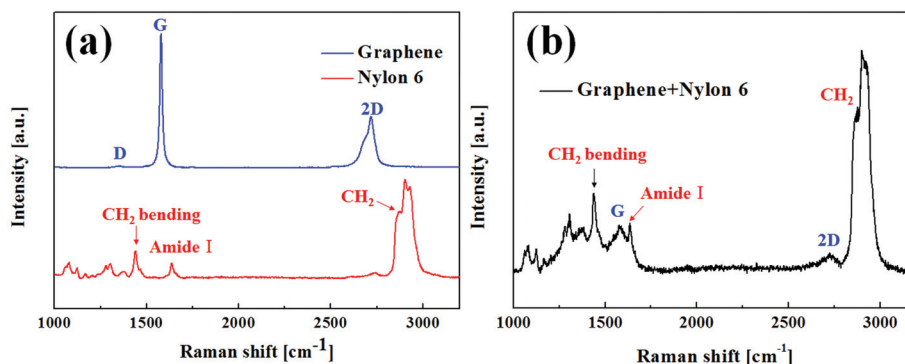


Fig. 6 Raman spectroscopy of the graphene–nylon-6 membrane.

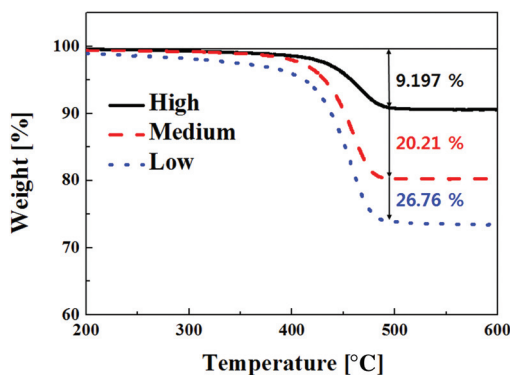


Fig. 7 TGA of nylon-6 nanofibers with (a) low, (b) medium, and (c) high concentrations of graphene.

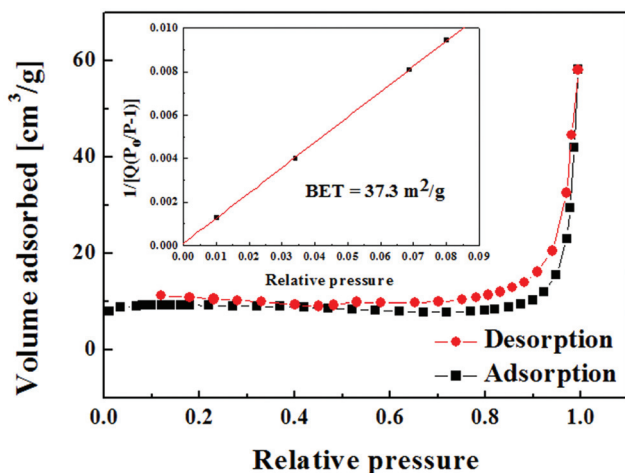


Fig. 8 The nitrogen adsorption–desorption isotherm of low graphene/nylon-6 composite.

porous and mesoporous nature of the sample. The vertical turn up between the relative pressure of 0.9 and 1.0 could be due to the additional macroporous structure.³⁴ The overall specific surface area (SSA) obtained by BET fitting of the iso-

therm is $37.3 \text{ m}^2 \text{ g}^{-1}$, quite low compared to the high theoretical SSA of pure graphene. This modest SSA can be attributed to stacking of graphene flakes, the multi-layer nature of the graphene used here, and the presence of nylon-6 fibers in the sample.³⁴ The graphene flakes used here have a typical thickness of 6 to 8 nm and a SSA of 120 to $150 \text{ m}^2 \text{ g}^{-1}$. The SSA of the membrane is 25–30% of the SSA of the graphene component alone.

3.2 Water purification by adsorption in the nanocomposite membrane

Fig. 9 compares the decolorization capability, *via* adsorption, of our low, medium, and high concentration membranes, which were previously considered in Fig. 2 and 7. Here, “*M*” refers to the locations in the stream-wise direction. The original methylene blue (MB) solution is injected from the left to right, and is removed as the solution passes through each of the membranes installed in the stainless steel fittings. $M = 0$ and $M = 1$ refer to the original and the decolorized MB solutions after passing the first membrane, respectively. As Fig. 9 shows, the low graphene concentration membrane, (a), yielded the lowest purification of all three membranes and the snapshot reveals that the solution is not completely purified, even at $M = 3$. This result is reflected in the corresponding absorbance data; *i.e.*, the MB solution concentration decreases progressively with increasing distance downstream. This trend is also confirmed for the medium (b) and high (c) concentration cases where complete purification is achieved after the third ($M = 3$) and second ($M = 2$) membranes, respectively. Therefore, the best purification performance is obtained with the membrane of the highest graphene concentration.

The excellent electronic, thermal, and mechanical properties of graphene with giant π -conjugation are derived from its sp^2 -hybridized layers and honey-comb-like structure. Moreover, its large surface area could produce outstanding adsorptivity and in turn, excellent purification ability. As mentioned above, the SSA (specific surface area) of the membrane with low graphene loading was $37 \text{ m}^2 \text{ g}^{-1}$, much lower than the theoretical surface area of single-layer graphene, and just 25 to 30% of the SSA of the graphene starting material. In the

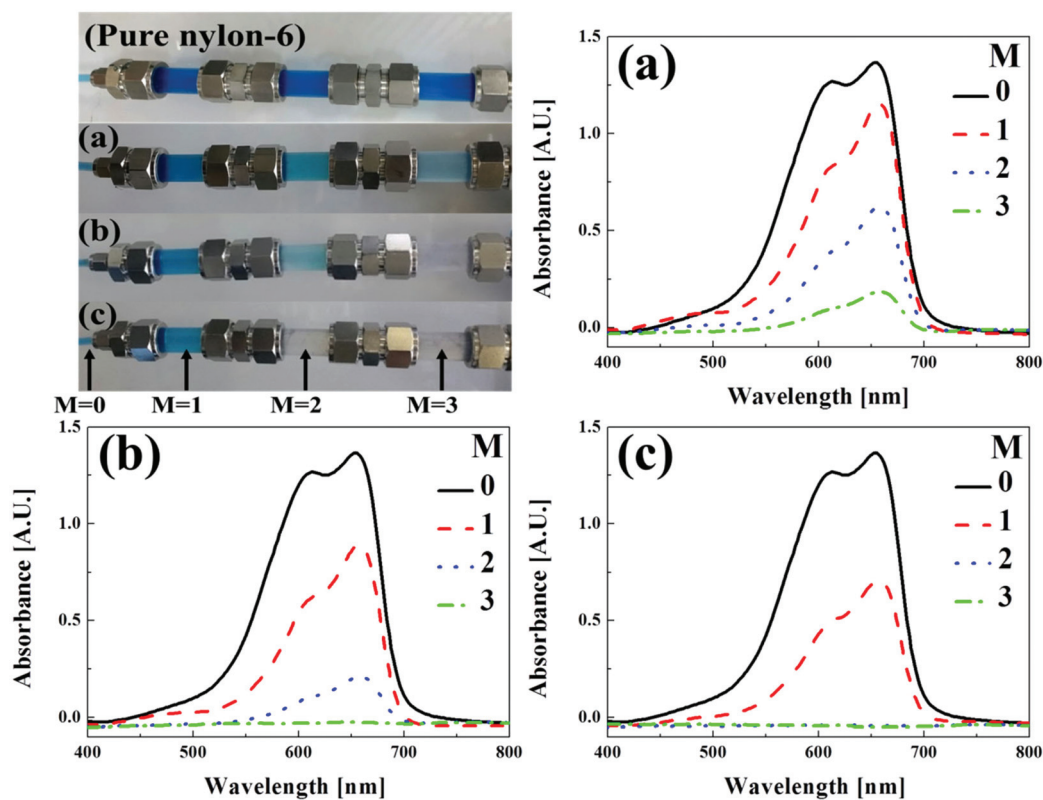


Fig. 9 Decolorization and absorbance of 1 wt% MB solution by the (a) low, (b) medium, and (c) high concentration membranes. The flow rate was 0.6 mL min^{-1} through a membrane diameter of 12.5 mm.

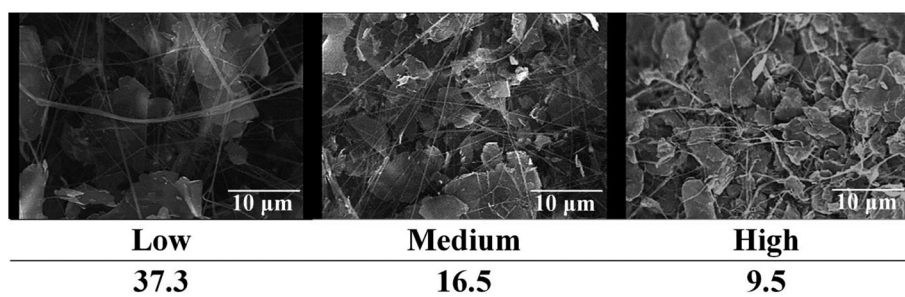


Fig. 10 BET surface area ($\text{m}^2 \text{ g}^{-1}$) of the low, medium, and high graphene loaded nylon-6 membranes.

graphene/nylon-6 membrane, some portion of the graphene surface area is blocked by the nylon nanofibers. In addition, the nanofibers themselves add mass to the sample while adding a comparatively little surface area. Fig. 10 depicts the BET surface area of the low, medium, and high graphene loaded nylon-6 membranes. The BET specific surface area of the membranes decreases with the increased loading of graphene from low to high. This is because of the strong accumulation of graphene which densifies the membrane. The high speed impact of graphene flakes at longer deposition times squeezes the deposited graphene flakes and therefore their

exposed areas are reduced, resulting in a reduction in the surface area of the membrane at higher graphene loading. However, the overall concentration of the graphene in the membrane and the membrane thickness increased considerably from the low to high graphene/nylon-6 membrane. Therefore, with increasing membrane thickness and the total mass of graphene in the membrane, the number of MB binding sites increased, which eventually led to better separation of the MB from water. As shown in Fig. 9, the best performance for MB adsorption was obtained for high graphene concentration membranes. This is attributed to their larger number of

binding sites for MB adsorption compared to the membranes which have low and medium graphene concentrations.

Adsorption of MB on the graphene surface arises from the hydrophobic and lipophilic nature of graphene that exhibits a preferential sorption capacity towards organic MB molecules. Graphene is composed mainly of aromatic carbon-carbon bonds, which are rich in π -electrons. Thus, strong interactions between the MB molecules and graphene are attributed to π - π stacking between the aromatic rings in the MB molecule and the graphene surface. The MB dye molecules adhere to the surface of the graphene sheets with an offset face-to-face orientation *via* π - π stacking interactions, during which external mass transfer between the MB solution and the graphene sheets and boundary layer diffusion occur.²⁰

Graphene has, in addition to outstanding adsorption capability, higher water permeability than other carbon-based materials such as carbon nanotubes.^{35,36} Suk and Aluru³⁷ computed the water permeation through graphene by calculating the energy barrier for water transport. In that work, the graphene membrane was found to have a lower energy barrier for water transport compared to that of other membranes such as carbon nanotubes. In the present study, the energy barrier decreased with increased graphene loading, thereby resulting in the transport of larger amounts of water than that transported at high-energy barriers. The graphene/nylon-6 membranes could be regenerated by electrical treatment after each adsorption cycle to improve their lifespan. An *et al.* described the regeneration of the membranes by applying 10 kV voltage.³⁸ This voltage treatment induced MB molecules to detach from graphene, permitting the reuse of the membranes. This graphene membrane can potentially be implemented with electrical treatment for regeneration of the membranes.

Fig. 11 demonstrates the practicality of this membrane for use in large-scale systems. We increased the size of the membrane installed in the stainless steel fitting, which in this case has an inner diameter of 1 inch (note that the previous one used in Fig. 8 had an inner diameter of 0.5 inches). We also increased the flow rate of the syringe pump from 0.6 to

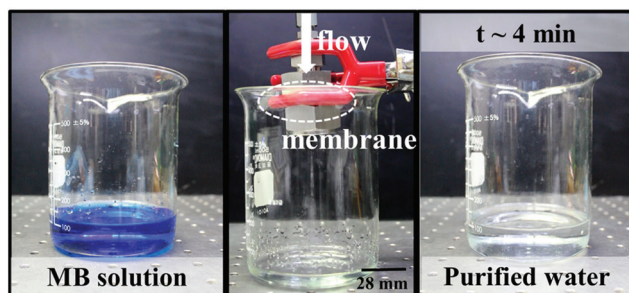


Fig. 11 Decoloration of an aqueous methylene blue (MB) solution by MB adsorption on the nanocomposite membrane. The flow rate was 30 mL min^{-1} . The permeability of this membrane was $4050 \text{ L h}^{-1} \text{ m}^{-2} \text{ bar}^{-1}$. The diameter of the membrane was 25.4 mm.

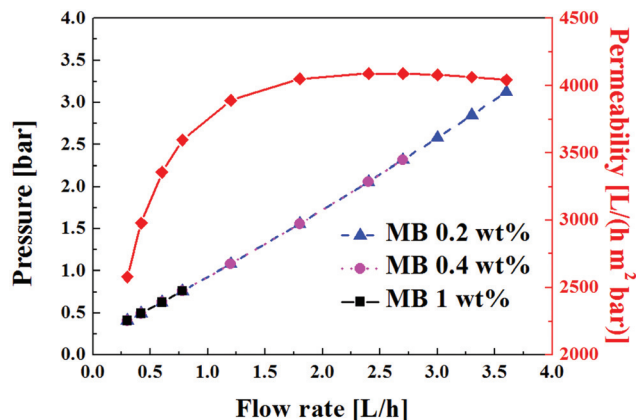


Fig. 12 Variation in pressure drop and permeability as a function of flow rate. Permeability is defined as the flow rate divided by the pressure and the cross-sectional area of the membrane. Note that $1 \text{ L h}^{-1} \sim 17 \text{ mL min}^{-1}$. The membrane diameter was 25.4 mm.

10 mL min^{-1} and installed 3 syringe pumps in order to yield a total flow rate of 30 mL min^{-1} . The membrane successfully purified the MB solution at a flow rate of 30 mL min^{-1} .

Fig. 12 shows the variation of the pressure drop across the membrane and the membrane permeability as a function of fixed flow rate; see the water purification movie from which the data in Fig. 12 were obtained in the ESI.† The pressure was increased by increasing the force exerted on the syringe pump with the given membrane which we used for this experiment. The permeability is in the range of a few thousand $\text{L h}^{-1} \text{ m}^{-2} \text{ bar}^{-1}$. This throughput value can be controlled by controlling the pore size of the membrane. From the previous SEM image in Fig. 2, we see that the porosity of the membrane is at a sub-micron scale. This nano- to microscale porosity will allow the membrane to filter particles and bacteria from the water as well as to absorb organic compounds like MB. Reducing the pore size even further would allow the membrane to remove smaller scale contaminants and other organic compounds. However, this would come at the cost of lower throughput or higher pressure drop.

Fig. 13(a) and (b) show, respectively, the C 1s XPS spectrum of the graphene before (left) and after (right) water purification *via* the membrane. The binding energy peak at 284.6 eV is attributed to the backbone C-C bond of the sp^2 carbon atoms in the graphene sheet surface.³⁹ Moreover, the binding energies of 285.9, 287.2, and 289.1 eV are typically attributed to the C-O, C=O, and O=C-OH functional groups, respectively.⁴⁰ Spectra were also obtained after the experiments in order to determine the effect of adsorption on the binding energies of these functional groups. Comparing Fig. 13(a) and (b) confirms the excellent stability of the system; *i.e.*, except for the C-O bond whose binding energy is slightly higher (286.3 eV), the functional groups have identical pre- and post-adsorption binding energies. These results concur with those of previous studies.⁷

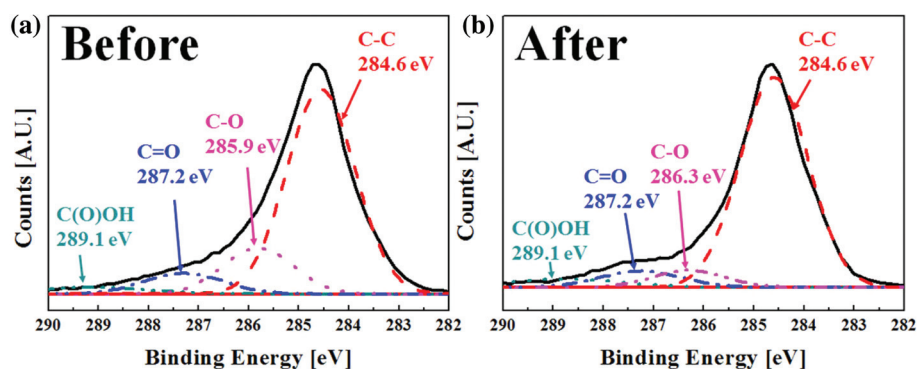


Fig. 13 C 1s deconvolution XPS peaks of graphene (a) before and (b) after adsorption.

4. Conclusion

A novel method of supersonic blowing for the fabrication of nylon-6 nanofibers entangled with graphene is described; membrane fabrication is quite simple and scalable for mass production. We used methylene blue as a model dye to demonstrate the adsorption ability of the nylon-6/graphene membranes. The corresponding results revealed that these membranes can be successfully applied for water purification. The high speed and simplicity of the fabrication method suggest that these membranes could be commercially viable. Furthermore, the membrane's high thermal stability as observed in TGA analysis and, most of all, the superior adsorption capacity can enable its practical application, especially in remote locations where potable water is scarce. These membranes can be directly applied for the purification of drinking water.

Acknowledgements

This research was supported by the Global Frontier Program through the Global Frontier Hybrid Interface Materials (GFHIM) of the National Research Foundation of Korea (NRF) funded by the Ministry of Science, ICT & Future Planning (2013M3A6B1078879) and NRF-2013R1A2A2A05005589. This work was supported by the Industrial Strategic Technology Development Program (10045221) funded by the Ministry of Knowledge Economy (MKE, Korea). The authors extend their appreciation to the Deanship of Scientific Research at King Saud University for funding this Prolific Research group (PRG-1436-03).

References

- Q. Bao, H. Zhang, J.-x. Yang, S. Wang, D. Y. Tang, R. Jose, S. Ramakrishna, C. T. Lim and K. P. Loh, *Adv. Funct. Mater.*, 2010, **20**, 782–791.
- S. An, B. N. Joshi, M. W. Lee, N. Y. Kim and S. S. Yoon, *Appl. Surf. Sci.*, 2014, **294**, 24–28.
- B. Arash, Q. Wang and V. K. Varadan, *Sci. Rep.*, 2014, **4**, 6479.
- Z. Xu and C. Gao, *Macromolecules*, 2010, **43**, 6716–6723.
- D. Cohen-Tanugi and J. C. Grossman, *Nano Lett.*, 2012, **12**, 3602–3608.
- H. Zhang, X. Lv, Y. Li, Y. Wang and J. Li, *ACS Nano*, 2009, **4**, 380–386.
- S. S. Gupta, T. S. Sreeprasad, S. M. Maliyekkal, S. K. Das and T. Pradeep, *ACS Appl. Mater. Interfaces*, 2012, **4**, 4156–4163.
- T. Liu, Y. Li, Q. Du, J. Sun, Y. Jiao, G. Yang, Z. Wang, Y. Xia, W. Zhang, K. Wang, H. Zhu and D. Wu, *Colloids Surf., B: Biointerfaces*, 2012, **90**, 197–203.
- C. A. Crock, A. R. Rogensues, W. Shan and V. V. Tarabara, *Water Res.*, 2013, **47**, 3984–3996.
- Z. Sui, Q. Meng, X. Zhang, R. Ma and B. Cao, *J. Mater. Chem.*, 2012, **22**, 8767–8771.
- G. Singh, D. Rana, T. Matsuura, S. Ramakrishna, R. M. Narbaitz and S. Tabe, *Sep. Purif. Technol.*, 2010, **74**, 202–212.
- E. N. Wang and R. Karnik, *Nat. Nanotechnol.*, 2012, **7**, 552–554.
- D. Konatham, J. Yu, T. A. Ho and A. Striolo, *Langmuir*, 2013, **29**, 11884–11897.
- M. Xue, H. Qiu and W. Guo, *Nanotechnology*, 2013, **24**, 505720.
- C. Zhu, H. Li, X. C. Zeng, E. G. Wang and S. Meng, *Sci. Rep.*, 2013, **3**, 3163.
- R. Das, M. E. Ali, S. B. A. Hamid, S. Ramakrishna and Z. Z. Chowdhury, *Desalination*, 2014, **336**, 97–109.
- J. Kou, X. Zhou, H. Lu, F. Wu and J. Fan, *Nanoscale*, 2014, **6**, 1865–1870.
- B. Mi, *Sci.*, 2014, **343**, 740–742.
- D. Cohen-Tanugi and J. C. Grossman, *J. Chem. Phys.*, 2014, **141**, 074704.
- H. Yoon, S.-H. Na, J.-Y. Choi, S. S. Latthe, M. T. Swihart, S. S. Al-Deyab and S. S. Yoon, *Langmuir*, 2014, **30**, 11761–11769.

- 21 E. S. Medeiros, G. M. Glenn, A. P. Klamczynski, W. J. Orts and L. H. Mattoso, *J. Appl. Polym. Sci.*, 2009, **113**, 2322–2330.
- 22 S. Sinha-Ray, A. L. Yarin and B. Pourdeyhimi, *Carbon*, 2010, **48**, 3575–3578.
- 23 S. Sinha-Ray, Y. Zhang, A. Yarin, S. Davis and B. Pourdeyhimi, *Biomacromolecules*, 2011, **12**, 2357–2363.
- 24 S. Sinha-Ray, M. W. Lee, S. Sinha-Ray, S. An, B. Pourdeyhimi, S. S. Yoon and A. L. Yarin, *J. Mater. Chem. C*, 2013, **1**, 3491–3498.
- 25 D.-Y. Kim, J.-J. Park, J.-G. Lee, D. Kim, S. J. Tark, S. Ahn, J. H. Yun, J. Gwak, K. H. Yoon, S. Chandra and S. S. Yoon, *J. Therm. Spray Technol.*, 2013, **22**, 1092–1102.
- 26 D. Y. Kim, S. Sinha-Ray, J. J. Park, J. G. Lee, Y. H. Cha, S. H. Bae, J. H. Ahn, Y. C. Jung, S. M. Kim, A. L. Yarin and S. S. Yoon, *Adv. Funct. Mater.*, 2014, **24**, 4986–4995.
- 27 D.-Y. Kim, J.-G. Lee, B. N. Joshi, S. S. Latthe, S. S. Al-Deyab and S. S. Yoon, *J. Mater. Chem. A*, 2015, **3**, 3975–3983.
- 28 A. Bianco, H.-M. Cheng, T. Enoki, Y. Gogotsi, R. H. Hurt, N. Koratkar, T. Kyotani, M. Monthieux, C. R. Park, J. M. D. Tascon and J. Zhang, *Carbon*, 2013, **65**, 1–6.
- 29 H. R. Pant, M. P. Bajgai, K. T. Nam, K. H. Chu, S.-J. Park and H. Y. Kim, *Mater. Lett.*, 2010, **64**, 2087–2090.
- 30 H. R. Pant, M. P. Bajgai, K. T. Nam, Y. A. Seo, D. R. Pandeya, S. T. Hong and H. Y. Kim, *J. Hazard. Mater.*, 2011, **185**, 124–130.
- 31 J. Zhao, H. Li, Z. Liu, W. Hu, C. Zhao and D. Shi, *Carbon*, 2015, **87**, 116–127.
- 32 M. M. Herbert, R. Andrade, H. Ishida, J. Maia and D. A. Schiraldi, *Polymer*, 2013, **54**, 6992–7003.
- 33 S. V. Levchik, E. D. Weil and M. Lewin, *Polym. Int.*, 1999, **48**, 532–557.
- 34 A. B. Bourlinos, T. A. Steriotis, M. Karakassides, Y. Sanakis, V. Tzitzios, C. Trapalis, E. Kouvelos and A. Stubos, *Carbon*, 2007, **45**, 852–857.
- 35 O. G. Apul, Q. Wang, Y. Zhou and T. Karanfil, *Water Res.*, 2013, **47**, 1648–1654.
- 36 E. N. El Qada, S. J. Allen and G. M. Walker, *Chem. Eng. J.*, 2006, **124**, 103–110.
- 37 M. E. Suk and N. Aluru, *J. Phys. Chem. Lett.*, 2010, **1**, 1590–1594.
- 38 S. An, H. S. Jo, K. Y. Song, M. G. Mali, S. S. Al-Deyab and S. S. Yoon, *Nanoscale*, 2015, DOI: 10.1039/C5NR05005G, Accepted Manuscript.
- 39 Y. Zhang and C. Pan, *J. Mater. Sci.*, 2011, **46**, 2622–2626.
- 40 C. Mattevi, G. Eda, S. Agnoli, S. Miller, K. A. Mkhoyan, O. Celik, D. Mastrogiovanni, G. Granozzi, E. Garfunkel and M. Chhowalla, *Adv. Funct. Mater.*, 2009, **19**, 2577–2583.